

Fibroblast Growth Factor Homologous Factors Control Neuronal Excitability through Modulation of Voltage-Gated Sodium Channels

Mitchell Goldfarb,^{1,2,*} Jon Schoorlemmer,^{2,7} Anthony Williams,¹ Shyam Diwakar,^{3,4} Qing Wang,⁵ Xiao Huang,¹ Joanna Giza,¹ Dafna Tchetchik,¹ Kevin Kelley,² Ana Vega,⁶ Gary Matthews,⁶ Paola Rossi,³ David M. Ornitz,⁵ and Egidio D'Angelo³

¹Department of Biological Sciences, Hunter College of City University, New York, NY 10021, USA

²Department of Molecular, Cell and Developmental Biology, Mount Sinai School of Medicine, New York, NY 10029, USA

³Department of Physiological and Pharmacological Sciences, University of Pavia, Pavia, Italy

⁴Department of Mathematics, University of Milan, Milan, Italy

⁵Department of Molecular Biology and Pharmacology, Washington University School of Medicine, Saint Louis, MO 63110, USA

⁶Department of Neurobiology and Behavior, State University of New York, Stony Brook, NY 11794, USA

⁷Present address: Department of Cell and Developmental Biology, Centro de Investigaciones Biológicas (CIB/CSIC), Madrid 28040, Spain.

*Correspondence: goldfarb@genectr.hunter.cuny.edu

DOI 10.1016/j.neuron.2007.07.006

SUMMARY

Neurons integrate and encode complex synaptic inputs into action potential outputs through a process termed “intrinsic excitability.” Here, we report the essential contribution of fibroblast growth factor homologous factors (FHF), a family of voltage-gated sodium channel binding proteins, to this process. *Fhf1*^{-/-}*Fhf4*^{-/-} mice suffer from severe ataxia and other neurological deficits. In mouse cerebellar slice recordings, WT granule neurons can be induced to fire action potentials repetitively (~60 Hz), whereas *Fhf1*^{-/-}*Fhf4*^{-/-} neurons often fire only once and at an elevated voltage spike threshold. Sodium channels in *Fhf1*^{-/-}*Fhf4*^{-/-} granule neurons inactivate at more negative membrane potential, inactivate more rapidly, and are slower to recover from the inactivated state. Altered sodium channel physiology is sufficient to explain excitation deficits, as tested in a granule cell computer model. These findings offer a physiological mechanism underlying human spinocerebellar ataxia induced by *Fhf4* mutation and suggest a broad role for FHF in the control of excitability throughout the CNS.

INTRODUCTION

Neurons integrate and encode postsynaptic currents into outputs of action potentials for efficient information transmission along axons. The relationship between current input and action potential output, termed “intrinsic excitability,” is dependent upon the subcellular distribution

and biophysical properties of voltage-gated sodium channels. Resting sodium channels concentrated at the axon initial segment sense threshold depolarization in the neural soma and open rapidly to allow sodium influx and the rise in membrane potential representing the upstroke of the action potential. Fast inactivation of sodium channels along with gated potassium efflux mediate the rapid downstroke repolarization and afterhyperpolarization of the action potential. Thereafter, several physiological events, including the recovery of sodium channels from the inactivated state, determine if and when the axon initial segment can initiate the next action potential.

While the pore-forming α subunit of a voltage-gated sodium channel is inherently capable of undergoing voltage-dependent activation and inactivation (Catterall, 2000), protein-protein interactions and posttranslational modifications modulate the distribution and response characteristics of the channel. Sodium channel β subunits facilitate transfer of the α subunit from transport vesicles to cell surface membrane and also modulate the voltage dependence of channel activation, inactivation, and resurgent currents (Chen et al., 2002; Grieco et al., 2005; Isom et al., 1995; Patton et al., 1994; Spanpanato et al., 2004). Site-specific phosphorylation of α subunits by protein kinase A, protein kinase C, p38 stress kinase, or Fyn tyrosine kinase provides a means for signal transduction to modulate sodium channel response characteristics (Ahern et al., 2005; Cantrell and Catterall, 2001; Wittmack et al., 2005). Recently, fibroblast growth factor homologous factors (FHF) have been identified as another class of α subunit-binding proteins (Liu et al., 2001, 2003; Wittmack et al., 2004).

FHF comprise a family of vertebrate proteins related in sequence and structure to fibroblast growth factors (FGFs) (Goldfarb, 2005). While FHF are sometimes referred to by FGF nomenclature (FHF1 = FGF12, FHF2 = FGF13, FHF3 = FGF11, FHF4 = FGF14), FHF and prototypic FGFs

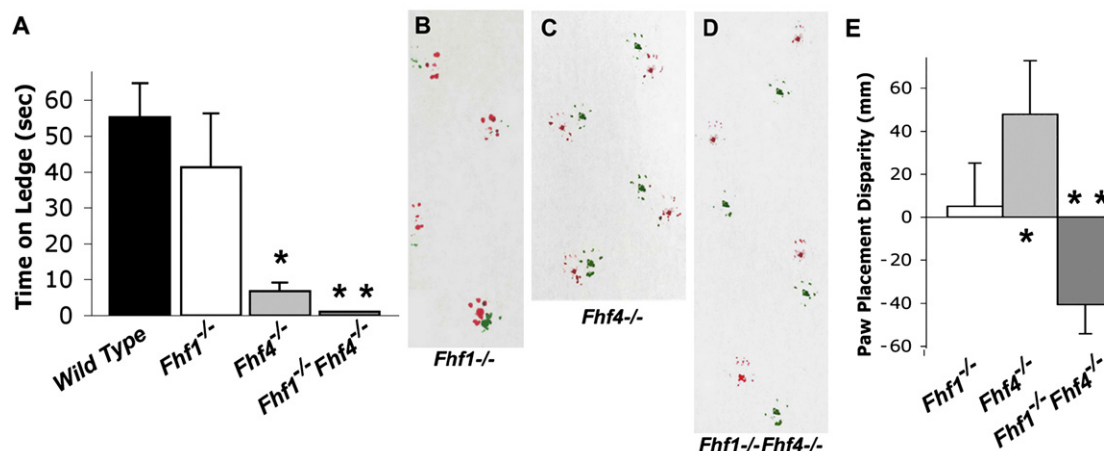


Figure 2. Motor Coordination Assays

(A) Ledge test. Mice were placed on a high, narrow ledge and timed until fall up to a maximum of 60 s. Significance of time differences in mutant mouse groups were analyzed by ANOVA for significance ($p < 0.05$). *, *Fhf4*^{-/-} mice significantly worse than wild-type; **, *Fhf1*^{-/-}*Fhf4*^{-/-} mice performed significantly worse than wild-type or *Fhf4*^{-/-}.

(B–E) Gait test. Paws of mice were painted (forepaws red, hindpaws green) and their footprints recorded while walking through a 7 cm diameter horizontal cylinder. Representative footprints from *Fhf1*^{-/-} (B), *Fhf4*^{-/-} (C), and *Fhf1*^{-/-}*Fhf4*^{-/-} (D) mice are shown, along with analysis of hindpaw misplacement along the forward axis (E). *, *Fhf4*^{-/-} mice significantly impaired in comparison to *Fhf1*^{-/-}; **, *Fhf1*^{-/-}*Fhf4*^{-/-} mice significantly worse than *Fhf4*^{-/-}.

mice properly superimposed their hindpaws onto sites where their forepaws were previously placed (Figure 2B). Last, *Fhf1*^{-/-} and wild-type mice performed similarly in a quantitative measurement of forelimb grip strength (data not shown). In contrast, *Fhf4*^{-/-} mice on the same strain background (C57Bl/6 × 129/Svev hybrid backcrossed two generations to 129/Svev) could not maintain their grip on an inverted grid (Figure S1), showed shorter ledge retention time (Figure 2A), and often failed to position their hindpaws properly during walking (Figures 2C and 2E). These deficiencies are consistent with ataxia and motor weakness, as had been previously shown for *Fhf4*^{-/-} mice on a predominantly C57Bl/6 background (Wang et al., 2002).

Fhf1 and *Fhf4* genes are normally expressed in partially overlapping sets of neurons in the central nervous system, including cerebellar granule neurons (Smallwood et al., 1996; Wang et al., 2000). We reasoned that mice lacking functional alleles for both of these genes could display accentuated and novel behavioral deficits in comparison to *Fhf4*^{-/-} animals. Indeed, *Fhf1*^{-/-}*Fhf4*^{-/-} mice showed more severe ataxia and motor weakness. They could not retain themselves on a narrow ledge for any measurable time (Figure 2A), they displayed a highly abnormal gait, often placing their hindpaws in front of their previously positioned forepaws (Figures 2D and 2E), they rapidly stumbled off of a metal grid tilted to only a 45° diagonal (Figure S1), and could not hold on to a rod with any measurable force when pulled backward by the tail (data not shown). Additionally, *Fhf1*^{-/-}*Fhf4*^{-/-} mice showed increased locomotor activity when disturbed or placed in a new environment, a phenotype not observed in mice

bearing even one functional allele of either *Fhf* gene. This behavior could be quantitated by counting revolutions that mice performed when placed in a small circular container (Figure S2). Overall, these experiments revealed functional requirements for FHF1 when FHF4 was absent.

Normal Cerebellar Architecture and Granule Neuron Morphology in *Fhf1*^{-/-}*Fhf4*^{-/-} Mice

Functional deficits in *Fhf1*^{-/-}*Fhf4*^{-/-} mice were apparent at weaning and did not noticeably progress in severity as animals aged. Furthermore, mutant animals never died of natural causes past weaning over the maximum 1 year time span that they were maintained. Histological evaluation of cerebellum in a 6-month-old mutant mouse was unremarkable; the internal granule cell layer and Purkinje cells were well formed, and Luxol Fast blue staining of myelin in fiber tracts beneath the cortex was apparent (Figures 3A and 3B). Confocal immunofluorescence showed that axon initial segments of granule neurons in the cerebellum of an *Fhf1*^{-/-}*Fhf4*^{-/-} mouse possess sodium channel Na_v1.6 (Figures 3C–3H), the channel which only appears at an advanced stage of granule neuron maturation (Osorio et al., 2005). Cerebellar granule neurons from *Fhf1*^{-/-}*Fhf4*^{-/-} pups maintained in culture for 30 days were indistinguishable from wild-type cultured cells in terms of both gross morphology under phase contrast microscopy (Figures 3I and 3J) and the presence of a well-formed axon initial segment bearing voltage-gated sodium channels (Figures 3K and 3L) that colocalize with ankyrin G (Figures 3M and 3N). In aggregate, these data argue against a developmental deficit or degenerative process in *Fhf* mutant animals.

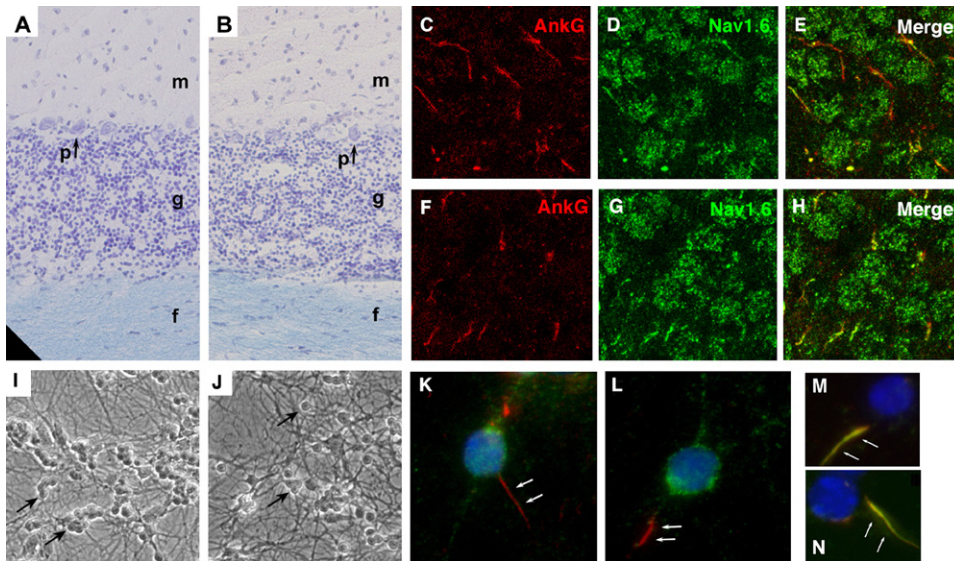


Figure 3. Cerebellar Histology and Granule Neuron Integrity in *Fhf1*^{-/-}*Fhf4*^{-/-} Mice

(A and B) Histology of wild-type (A) and *Fhf1*^{-/-}*Fhf4*^{-/-} (B) cerebellar cortex cryosections stained with cresyl violet, eosin Y, and Luxol Fast blue. m, molecular layer; g, internal granule layer; p, Purkinje cell soma; f, fiber layer.

(C–H) Confocal immunofluorescence detection of Na_v1.6 in cerebellar granule cells in situ. Cryosections of wild-type (C–E) and *Fhf1*^{-/-}*Fhf4*^{-/-} (F–H) granule layer were probed for axon initial segment marker ankyrin G (C and F) and Na_v1.6 (D and G); merged images (E and H).

(I and J) Phase contrast micrographs of P10 cerebellar neurons cultured for 21 days. Abundant small round-soma granule neurons (e.g., arrows) are discernable in wild-type (I) and *Fhf1*^{-/-}*Fhf4*^{-/-} (J) cultures.

(K–N) Immunofluorescence analysis of granule neurons cultured for 30 days. Wild-type (K and M) and *Fhf1*^{-/-}*Fhf4*^{-/-} (L and N) cells were stained with either anti-glutamate transporter EAAC1 (green) and anti-pan-sodium channel α (red) (K and L) or anti-pan-sodium channel α (green) and ankyrin G (red) (M and N) and counterstained with DAPI (blue). Surface and vesicular EAAC1 (K and L) visualizes cell soma and processes. Arrows point to axon initial segments. Overlapping ankyrin G and sodium channel staining (M and N) appears yellow.

FHF2s Are Present at the Axon Initial Segment

Native complexes of FHF2 in association with voltage-gated sodium channels have been detected in extracts from whole rat brain (Wittmack et al., 2004). In addition, we can detect complexes of FHF1 and sodium channels in extracts from mouse cerebellum (Figure 4A). To investigate whether FHF modulation of cerebellar granule neuron intrinsic excitability underlies ataxia of *Fhf* mutant mice, we first tested whether FHF proteins colocalize with sodium channels at the axon initial segment of granule neurons. Since suitable antibodies for immunostaining endogenous FHF1 or FHF4 are not available, cultured granule neurons were transfected with expression vectors for FHF1a or FHF1b fused to green fluorescent protein (GFP). As shown in Figures 4B–4G, FHF1a-GFP and FHF1b-GFP are detected in neuron soma and in the axon initial segment together with voltage-gated sodium channels. In order to confirm a similar localization for native FHF protein, we probed untransfected cultured hippocampal neurons with antibodies specific for FHF2, sodium channels, and ankyrin G, which demarcates the initial segment (Kordeli et al., 1995). Strong FHF2 immunoreactivity was detectable in the neural soma and in the axon initial segment (Figures 3H–3M). Immunostaining of axon initial segments with the FHF2 antibodies was suppressed by preincubation with the immunizing FHF2

peptide, but not with an unrelated peptide (data not shown), demonstrating the specificity of the staining. In aggregate, these findings show that a broad repertoire of FHF isoforms colocalize with sodium channels at the axon initial segment and are good candidates to serve as modulators of intrinsic excitability.

Excitability Deficits in FHF Mutant Cerebellar Granule Neurons

The intrinsic excitability of cerebellar granule neurons in juvenile (20- to 30-day-old) rats and mice has been studied extensively. In response to sufficient sustained inward current injection through a patch pipette, these cells respond with a continuous train of action potentials at frequencies up to 50–150 Hz (Chadderton et al., 2004; D'Angelo et al., 1998; Gall et al., 2003). Intrinsic excitability of granule cells in adult (3- to 12-month-old) mouse brain slices was examined here by blind whole-cell patch-clamp in current-clamp mode, applying inward current of various amplitudes for the duration of 800 ms. Suitable brain slice preparations were only achieved through the application of reagents to the tissue dissection and incubation solutions preventing N-methyl-D-aspartate receptor transmission and rapid neuronal cell death (see Experimental Procedures). Patched cells were confirmed as granule neurons by their measured membrane

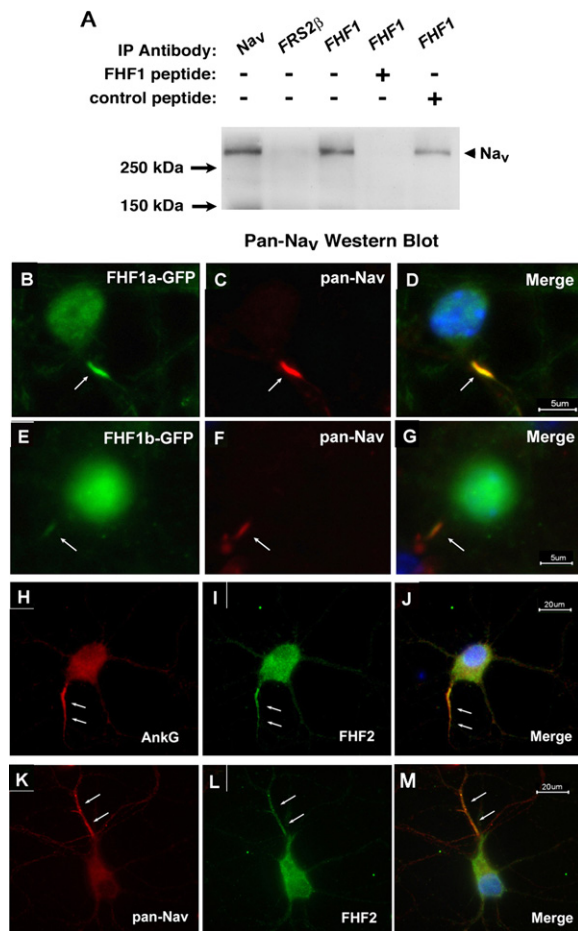


Figure 4. FHF Proteins Localize to the Axon Initial Segment and Associate with Sodium Channels

(A) FHF1/sodium channel complexes in cerebellum. Triton X-100 extracts of mouse cerebellum were immunoprecipitated with pan-sodium channel α subunit monoclonal antibody, rabbit anti-FHF1, or rabbit anti-FRS2 β . For FHF1 immunoprecipitation, the antibodies were preincubated with the immunizing FHF1 12-mer peptide, a non-specific 12-mer peptide, or no peptide. Captured immunoprecipitates were electrophoresed on a 7.5% polyacrylamide-SDS gel, blot transferred, and probed with pan-sodium channel monoclonal antibody. Migration of molecular weight standards is indicated (arrows), as is the position of detected sodium channel (arrowhead). The specificity of FHF1/channel coprecipitation is established by loss of pull-down when anti-FHF1 is preincubated with immunizing peptide, but not with an alternative peptide, and by virtual absence of precipitation using the unrelated anti-FRS2 β antibody raised and purified by identical procedures.

(B–G) FHF1-GFP fusion proteins localize to cerebellar granule neuron axon initial segment. Wild-type mouse granule cells cultured for 18 days were transfected with expression constructs for GFP fused to mouse FHF1a (B–D) or human FHF1b (E–G). After 24 hr, cells were fixed and incubated with anti-GFP (mouse IgG2a) and anti-pan-sodium channel α (mouse IgG1), and bound antibodies were visualized by indirect immunofluorescence with biotinylated anti-mIgG2a + streptavidin-Alexa 488 (B and E) and Alexa 594-conjugated anti-mIgG1 (C and F). Merged images (D and G) include DAPI nuclear stain.

(H–M) Native FHF localizes to axon initial segment. Rat hippocampal neurons in primary culture for 12 days were fixed and incubated with

capacitance (C_m) of 2.5–6.0 pF, lack of spontaneous firing, and their generation of inward (sodium) and outward (potassium) currents following depolarization in voltage clamp (see below).

Above a minimum amplitude of injected current, all wild-type adult mouse granule neurons generated action potentials that increased in frequency with increased current amplitude. Maximum frequencies averaged 60 Hz (Figures 5A–5C), an example of which is shown in Figure 5D. The depolarization voltage threshold for spike generation was -49.6 ± 4.9 mV, and the amount of injected current needed to achieve threshold voltage varied among cells, reflecting their varying input resistance ($R_{in} = 1.53 \pm 0.7$ G Ω) (Table 1A). Input resistance variability is in part the consequence of patch seal weakening upon whole-cell break-in. The wild-type neurons also varied in their current-to-spike relationship; some cells showed graded excitability over a 2.5-fold range in injected current amplitude (Figure 5C, solid lines), while other cells gave closer to an all-or-nothing firing response (Figure 5C, dashed lines). The type of current-to-spike profile did not correlate with variations in R_{in} , C_m , or magnitude of voltage-gated currents and may reflect subtle differences in channel functionality or subcellular distribution among cells.

Granule neurons in *Fhf1*^{-/-} cerebella ($n = 4$) showed normal excitability, in terms of both maximum spike frequency and voltage threshold for spike induction (Figures 5A, 5B, and 5E and Table 1A). By contrast, no granule neurons in *Fhf4*^{-/-} or *Fhf1*^{-/-}*Fhf4*^{-/-} cerebella generated sustained repetitive firing. *Fhf4*^{-/-} cells ($n = 4$) generated an average maximum of approximately eight spikes, with most of these action potentials occurring within the first 100 ms of current injection (Figures 5A, 5B, and 5F and Table 1A). *Fhf1*^{-/-}*Fhf4*^{-/-} cells ($n = 7$) were more seriously impaired, averaging only two spikes maximum, with four of the seven recorded cells (57%) generating only a single early action potential (Figures 5A, 5B, and 5G and Table 1A). *Fhf1*^{-/-}*Fhf4*^{-/-} neurons displayed a significantly higher voltage threshold for spike generation (-40.6 ± 7.8 mV) than their wild-type counterparts (9 mV shift) and required greater injected current to depolarize to threshold voltage (Table 1A). These findings show a correlation between the magnitude of granule cell excitability deficits and degree of ataxia among *Fhf* mutant genotypes.

Mutant granule cells displayed a normal repertoire of voltage-gated currents. Upon voltage-clamped depolarization from -80 to -20 mV, wild-type and *Fhf1*^{-/-}*Fhf4*^{-/-} cells generated virtually the same amplitude of fast activating/inactivating inward current, which is predominantly a sodium current (Table 1A). Further depolarization

rabbit polyclonal anti-FHF2 antibodies (I and L) together with either anti-ankyrin G (mIgG1) (H) or anti-pan-sodium channel α (mIgG1) (K). Bound antibodies were visualized with biotinylated anti-rabbit IgG + streptavidin-Alexa 488 (I and L) and anti-mouse IgG-Alexa 594 (H and K). Merged images (J and M) include DAPI stain. Arrows denote axon initial segment.

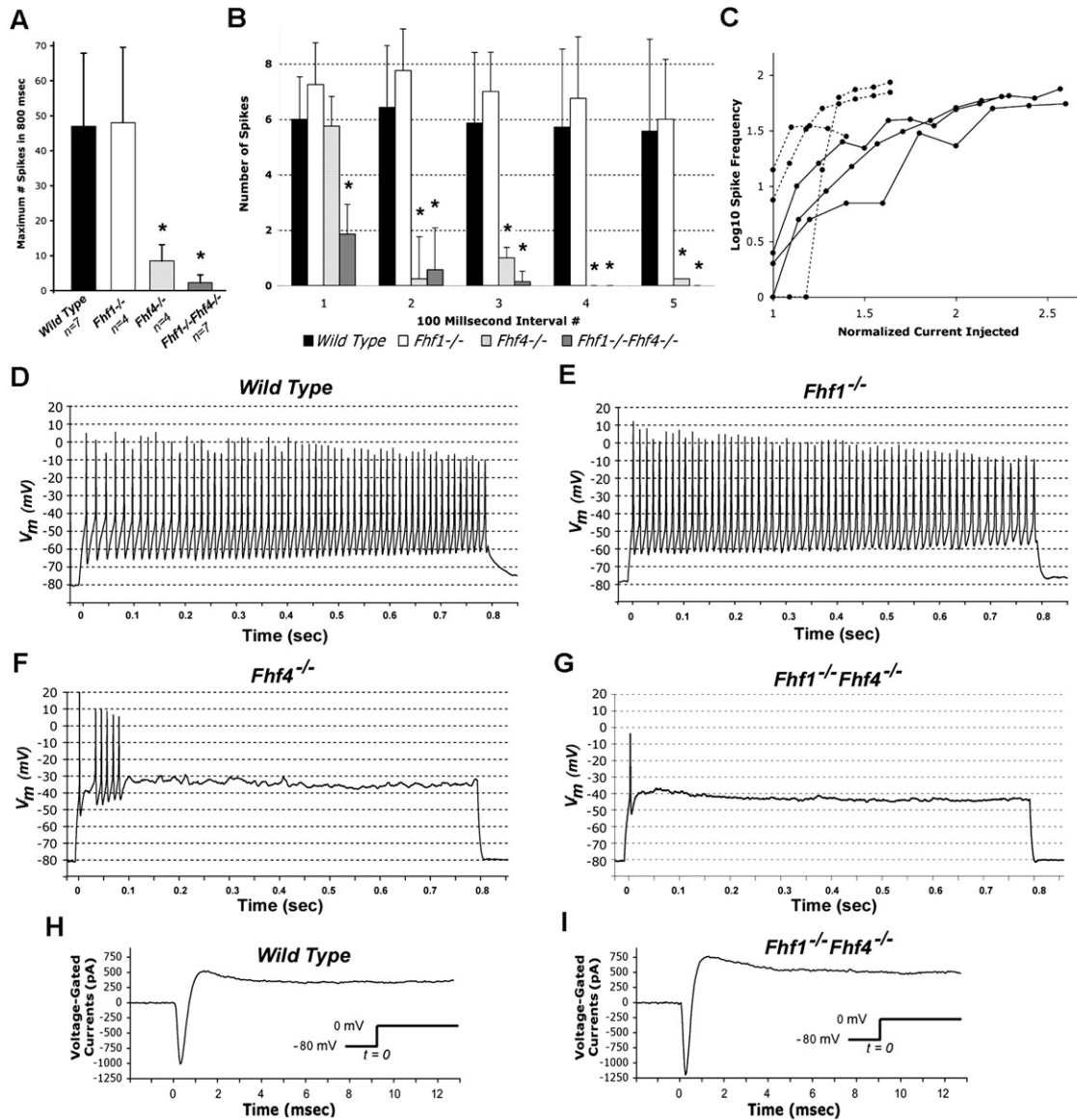


Figure 5. Intrinsic Excitability of Wild-Type and *Fhf* Mutant Granule Neurons from Brain Slice Preparations

(A) Maximal spike frequency for wild-type and mutant cells. For each patched granule neuron, current injection command sweeps of 800 ms duration and of different amplitudes were applied, action potentials recorded, and the maximum number spikes in any sweep determined. *n*, number of cells recorded in genotype. *, *Fhf4*^{-/-} and *Fhf1*^{-/-}*Fhf4*^{-/-} less excitable than wild-type (*p* < 0.01 by ANOVA).

(B) Distribution of spikes during 800 ms current injection. For sweep giving highest spike frequency in each cell, the number of spikes in each of the first five 100 ms intervals was counted. *, number of spikes during interval for mutant cells less than for wild-type cells (*p* < 0.05 by ANOVA).

(C) Current-to-spike relationship among wild-type neurons. For each cell, smallest injected current to generate any spikes was normalized to 1. —, cells displaying graded current-to-spike profile; - - - -, cells displaying steep current-to-spike profile.

(D–G) Membrane voltage recordings of representative cells for each genotype during current injection: (D) wild-type, (E) *Fhf1*^{-/-}, (F) *Fhf4*^{-/-}, (G) *Fhf1*^{-/-}*Fhf4*^{-/-}. Repetitive firing is impaired in the *Fhf4*^{-/-} neuron, and the *Fhf1*^{-/-}*Fhf4*^{-/-} neuron generated only one initial spike. Also note elevated voltage spike thresholds and afterhyperpolarizations in (F) and (G).

(H and I) Current traces of wild-type (H) and *Fhf1*^{-/-}*Fhf4*^{-/-} (I) cells following voltage-clamp depolarization from –80 to 0 mV (inset). Both cells generate typical fast inward inactivating current and both inactivating and noninactivating outward currents.

revealed similar amplitudes and kinetics of this inward current, followed by inactivating and noninactivating outward potassium currents (Figures 5H and 5I and Table 1A). The variable input resistance recorded among cells is

insufficient to account for the consistent deficit in repetitive firing and altered voltage spike threshold in mutant cells. For example, the wild-type and *Fhf1*^{-/-}*Fhf4*^{-/-} cells shown in Figures 5H and 5I had similar voltage-gated

Table 1. Summary of Electrophysiological Data

A. Cerebellar Slice Recordings—Physiological Solutions				
	Wild-Type	<i>Fhf1</i> ^{-/-}	<i>Fhf4</i> ^{-/-}	<i>Fhf1</i> ^{-/-} <i>Fhf4</i> ^{-/-}
# Cells recorded	7	4	4	7
R _{in} (GΩ)	1.53 ± 0.70	1.40 ± 0.42	0.47 ± 0.20	0.95 ± 0.51
C _m (pF)	4.62 ± 0.96	4.24 ± 1.40	4.47 ± 1.35	4.35 ± 1.16
R _s (MΩ)	26.6 ± 14.0	25.2 ± 7.2	19.1 ± 6.3	22.3 ± 8.9
I _{in-peak} at -10 mV (pA)	-1012 ± 287	-933 ± 360	-1860 ± 707	-1033 ± 359
I _{out-peak} at +20 mV (pA)	999 ± 421	844 ± 446	956 ± 440	974 ± 950
V _{rest} (mV)	-69.4 ± 8.4	-72.3 ± 4.9	-55.3 ± 10.7	-59.9 ± 6.3
V _{threshold} (mV)	-49.6 ± 4.9	-50.9 ± 9.8	-43.4 ± 4.4	-40.2 ± 8.7*
I _{threshold} × R _{in} (mV)	29.6 ± 6.5	27.4 ± 7.2	30.4 ± 4.6	39.4 ± 11.4
V _{ahp} (mV)	-59.8 ± 7.3	-61.9 ± 4.5	-50.4 ± 3.9	-46.8 ± 2.5*
Maximum # spikes in 800 ms	47.0 ± 20.9	48.0 ± 20.6	8.5 ± 4.7**	2.3 ± 2.2**#
B. Cultured Granule Cell Recordings—Sodium Currents Only				
	Wild-Type (# Cells)	<i>Fhf1</i> ^{-/-} <i>Fhf4</i> ^{-/-} (# Cells)	t Test	
C _m (pF)	4.74 ± 0.95 (9)	3.86 ± 0.83 (11)		
R _s (MΩ)	12.1 ± 3.5 (9)	13.5 ± 7.5 (11)		
Frequency voltage clamp (kHz)	2.99 ± 0.58 (9)	3.58 ± 0.95 (11)		
Transient I _{Na-Peak} at -15 mV (pA)	-431 ± 166 (9)	-536 ± 326 (11)		
Resurgent I _{Na} 5 mV to -85 mV (pA)	-117 ± 78 (9)	-134 ± 76 (9)		
Persistent I _{Na} at -35 mV (pA)	-26 ± 7 (9)	-12 ± 6 (9)	p < 0.0003	
V _{1/2} Activation (mV)	-33.3 ± 4.2 (9)	-36.5 ± 7.5 (11)		
k Activation (mV)	5.2 ± 0.7 (9)	4.6 ± 1.2 (11)		
V _{1/2} Inactivation (mV)	-59.1 ± 4.9 (8)	-72.8 ± 4.3 (9)	p < 0.00003	
k Inactivation (mV)	-5.8 ± 0.6 (8)	-5.3 ± 0.6 (9)		
τ _{Fast} Inactivation at -15 mV (msec)	1.10 ± 0.24 (6)	0.49 ± 0.08 (10)	p < 0.001	
τ _{Fast} Inactivation at -5 mV (msec)	0.64 ± 0.12 (6)	0.33 ± 0.05 (10)	p < 0.0003	
τ _{Recovery} at -85 mV (ms)	3.80 ± 0.80 (7)	5.88 ± 0.88 (7)	p < 0.001	
C. Cerebellar Slice Recordings—Sodium Currents Only				
	Wild-Type (# Cells)	<i>Fhf1</i> ^{-/-} <i>Fhf4</i> ^{-/-} (# Cells)	t Test	
C _m (pF)	4.58 ± 0.99 (14)	3.89 ± 0.67 (15)		
R _s (MΩ)	16.0 ± 6.7 (14)	17.9 ± 10.4 (15)		
Frequency voltage clamp (kHz)	2.61 ± 1.24 (14)	2.88 ± 1.03 (15)		
Transient I _{Na-Peak} at -15 mV (pA)	-907 ± 367 (11)	-551 ± 201 (10)	p < 0.02	
Resurgent I _{Na} 5 mV to -85 mV (pA)	-65 ± 46 (9)	-28 ± 26 (10)		
V _{1/2} Inactivation (mV)	-55.6 ± 2.0 (6)	-69.9 ± 5.3 (8)	p < 0.00005	
k Inactivation (mV)	-4.8 ± 0.9 (6)	-5.2 ± 0.9 (8)		
τ _{Recovery} at -85 mV (ms)	3.04 ± 0.20 (4)	7.22 ± 3.31 (6)	p < 0.025	

*Significant deficit (p < 0.05) by ANOVA. **Significant deficit (p < 0.01) by ANOVA. #Significant versus *Fhf4*^{-/-} (p < 0.05) by t test.

currents, R_{in} (0.81 versus 0.66 GΩ) and C_m (3.6 versus 4.0 pF), but still differed in repetitive firing (28 versus 1 spike maxima during current injection) and voltage threshold for spiking (-48 versus -40 mV).

Sodium Channel Inactivation Parameters Are Altered in *Fhf1*^{-/-}*Fhf4*^{-/-} Granule Neurons

The colocalization and physical interaction of FHF's with sodium channels suggested that intrinsic excitability

deficits in *Fhf* mutant granule neurons could reflect altered sodium channel physiology. Sodium channel response characteristics were monitored by voltage-clamp protocols using patch pipette and bath solutions that inhibit active currents other than sodium (calcium, potassium, and chloride) (Magistretti et al., 2006). Initial analyses were performed on cultured granule neurons (16–30 days in vitro), some of which afforded excellent voltage clamp of the axonal sodium conductance.

The voltage dependence of sodium channel activation was assayed by step depolarizations from a holding potential of -95 mV. Current traces and derived plots from representative wild-type and *Fhf1*^{-/-}*Fhf4*^{-/-} cells are shown in Figures 6A and 6B, and the averaged data for all cells are provided in Figure 6E and Table 1B. *Fhf* mutation induces a small, but insignificant, leftward shift in the voltage dependence of sodium channel activation (wild-type, -33.3 ± 4.3 mV; *Fhf1*^{-/-}*Fhf4*^{-/-}, -36.5 ± 7.5 mV; $p > 0.2$). Peak fast sodium current upon depolarization and resurgent current upon repolarization were variable among cells in both groups, and *Fhf* mutation did not cause detectable changes in current densities (Table 1B).

The voltage-dependence of sodium channel fast inactivation was analyzed by measuring peak sodium current induced at -15 mV subsequent to a 125 ms preconditioning voltage command. Current traces and derived plots from representative wild-type and *Fhf1*^{-/-}*Fhf4*^{-/-} cells are shown in Figures 6C and 6D, and the averaged data for all cells are provided in Figure 6E and Table 1B. *Fhf* mutation induced a highly significant 13–14 mV hyperpolarizing shift in the voltage dependence of channel inactivation (wild-type, -59.1 ± 4.8 mV; *Fhf1*^{-/-}*Fhf4*^{-/-}, -72.8 ± 4.3 mV; $p < 0.00003$). The shift in voltage-dependent inactivation reduces the so-called window current in *Fhf1*^{-/-}*Fhf4*^{-/-} cells (Figure 6E), suggesting that mutant cells would have reduced persistent sodium currents. Indeed, sodium currents persisting 25 ms after depolarization to -35 mV were substantially diminished among *Fhf1*^{-/-}*Fhf4*^{-/-} cells (wild-type, -26 ± 7 pA; *Fhf1*^{-/-}*Fhf4*^{-/-}, -12 ± 6 pA; $p < 0.0003$) (Figure 6F and Table 1B).

The hyperpolarizing shift in voltage-dependent fast inactivation of sodium channels might be expected to accelerate the rate of channel inactivation in *Fhf1*^{-/-}*Fhf4*^{-/-} cells. The rates of channel inactivation were calculated from the decay profile of sodium current amplitude following channel activation. As shown in Figure 7A and Table 1B, the inactivation rates of sodium channels at -15 or -5 mV were significantly faster in *Fhf1*^{-/-}*Fhf4*^{-/-} cells. Consequently, the sodium current peak is narrower in width for mutant cells (see example in Figure 7B).

$\text{Na}_v1.6$ sodium channels that predominate at the axon initial segment are known to undergo rapid recovery from inactivation following restoration of strong negative membrane potential (Herzog et al., 2003), and one isoform of FHF2 (FHF2a) has been reported to slow recovery (Rush et al., 2006). We have analyzed rates of sodium channel recovery in wild-type and *Fhf1*^{-/-}*Fhf4*^{-/-} granule neurons by subjecting cells to two 10 ms intervals of depolarization

to -15 mV separated by a -85 mV recovery period of variable test duration. The relative amplitude of the second induced sodium current following the recovery period indicated the fraction of channels recovered. Sodium channels in wild-type cells (example in Figure 7C) recovered from inactivation ($\tau_{\text{recovery}} = 3.80 \pm 0.80$ ms) significantly faster than did channels in *Fhf1*^{-/-}*Fhf4*^{-/-} cells ($\tau_{\text{recovery}} = 5.88 \pm 0.88$ ms; $p < 0.001$) (Figure 7E and Table 1B, example in Figure 7D).

A similar analysis of sodium channel physiology was conducted on granule neurons in adult cerebellum slice preparations. Attempts to analyze the voltage dependence of sodium channel activation were complicated by clear signs of clamp escape (Figures S3A and S3B), probably due to more remote localization of sodium channels in the axon initial segments of fully mature cells. Nevertheless, some channel parameters could be reliably recorded. Voltage-dependent fast inactivation displayed a -14 mV hyperpolarizing shift (Figure S3C and S3D and Table 1C) and a slowed rate of recovery from inactivation (Figures S3E and S3F and Table 1C) in *Fhf1*^{-/-}*Fhf4*^{-/-} cells, comparable to data recorded from cultured neurons.

Granule Neuron Computer Model: FHF Modulation of Sodium Channels Is Essential for Sustained Excitability

The altered inactivation of sodium channels in *Fhf1*^{-/-}*Fhf4*^{-/-} cells seemed sufficient to account for the substantial rise in spike voltage threshold and for the failure of such cells to fire action potentials repetitively. Pipette-delivered current, acting similarly to native excitatory postsynaptic current, depolarizes cells with a time constant ($C_m \times R_{in}$) on the order of 4–6 ms, such that sodium channels are vulnerable to inactivation during initial current injection. In mutant cells, sodium channel inactivation is more severe, and greater current would be required to depolarize the neuron faster and further to reach a threshold voltage for spiking. Following a first spike, several factors would combine to block repetitive firing in the mutant cell. The greater pipette current required for the first spike would oppose potassium currents to raise the afterhyperpolarization potential and, together with the negative shift in voltage dependence of channel inactivation, would strongly disfavor channel recovery. Furthermore, the slower rate of recovery would further reduce channel availability, thereby suppressing subsequent action potentials.

In order to substantiate a functional relationship between altered channel physiology and impaired excitability, a granule neuron computer model was employed (Figure 8) (D'Angelo et al., 2001). Sodium channel behavior was modeled as previously described (Khaliq et al., 2003; Magistretti et al., 2006; Raman and Bean, 2001), with inactivation governed by voltage-independent drain of channels into inactivated states (see Experimental Procedures). By enhancing the entry and retention of channels in the inactivated states, the model reproduced the most evident changes in sodium currents observed in *Fhf1*^{-/-}*Fhf4*^{-/-} mice. In particular, appropriate changes

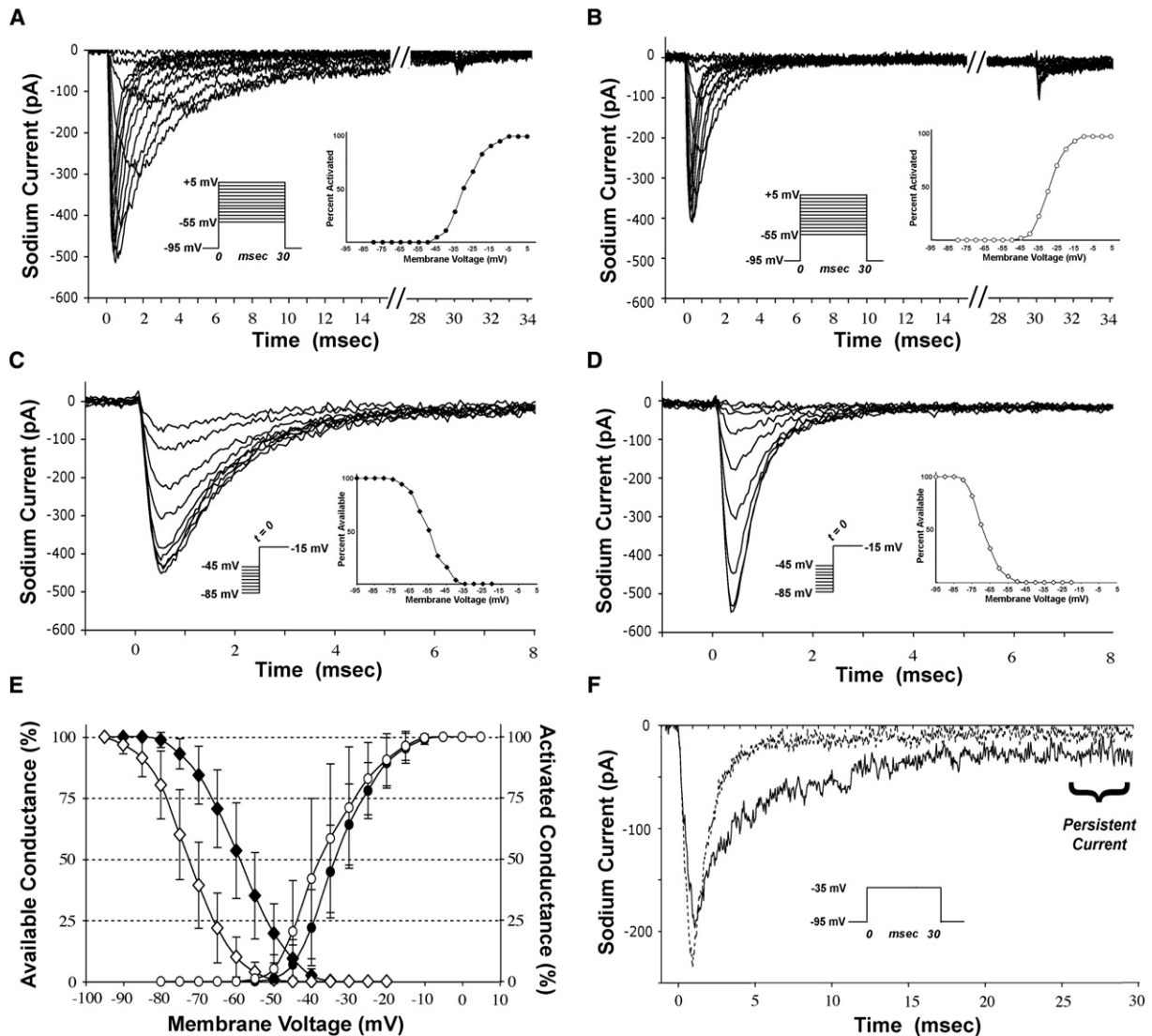


Figure 6. Voltage-Dependent Activation and Inactivation of Sodium Channels in Wild-Type and *Fhf1*^{-/-}*Fhf4*^{-/-} Cultured Granule Neurons

Recordings were in solutions only allowing for gated sodium currents.

(A) Sodium channel activation in a wild-type neuron. Superimposed current traces are from several voltage depolarization step commands from -85 mV holding potential (left inset). Peak conductance as a percentage of maximal conductance is plotted versus V_m (right inset).

(B) Sodium channel activation in a *Fhf1*^{-/-}*Fhf4*^{-/-} neuron. Voltage dependence of activation is similar to that of the wild-type cell (A).

(C) Sodium channel inactivation in a wild-type neuron. Superimposed current traces are from several voltage commands (left inset) consisting of a preconditioning voltage step (125 ms) followed by depolarization to -15 mV (only time frame bracketing the -15 mV depolarization is shown). Peak available conductance as a percentage of maximal conductance is plotted versus V_m (right inset).

(D) Sodium channel inactivation in a *Fhf1*^{-/-}*Fhf4*^{-/-} neuron. Voltage dependence of inactivation is shifted leftward more than 10 mV in comparison to transition in the wild-type cell (C).

(E) Voltage dependence of activation and inactivation for all recorded cells. The graph shows the average voltage dependence of channel activation in wild-type (closed circles, $n = 9$) and *Fhf1*^{-/-}*Fhf4*^{-/-} (open circles, $n = 11$) cells, together with average voltage dependence of channel inactivation in wild-type (closed diamonds, $n = 8$) and *Fhf1*^{-/-}*Fhf4*^{-/-} (open diamonds, $n = 9$) cells. The 13–14 mV negative shift for voltage-dependent channel inactivation in *Fhf1*^{-/-}*Fhf4*^{-/-} cells is highly significant ($p < 0.00003$).

(F) Persistent sodium currents. Current traces for a representative wild-type (solid line) and *Fhf1*^{-/-}*Fhf4*^{-/-} (dappled line) cell following depolarization to -35 mV illustrate current persisting after 25 ms, which is reduced in the mutant.

in kinetic constants accelerated current decay kinetics reducing τ_{decay} from 0.6 to 0.3 ms at -10 mV (Figure 8A), shifted steady-state inactivation by 10 mV to the left (Fig-

ure 8B), reduced the persistent sodium current (Figure 8A), and slowed recovery from inactivation (Figure 8B). Since inactivation limits the number of channels reaching the

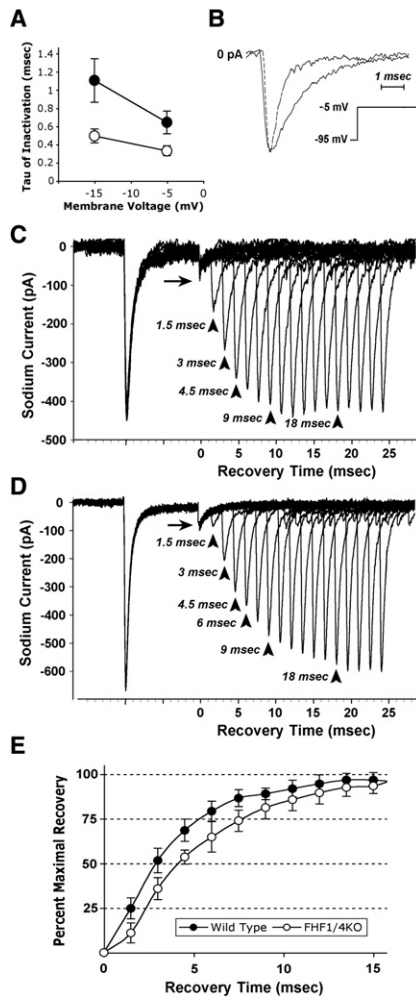


Figure 7. Rate Constants for Sodium Channel Inactivation and Recovery in Wild-Type and *Fhf1*^{-/-}*Fhf4*^{-/-} Cultured Granule Neurons

Recordings were in solutions only allowing for gated sodium currents. (A) Rates of inactivation. Wild-type (n = 6) and *Fhf1*^{-/-}*Fhf4*^{-/-} (n = 10) granule cells were depolarized to different voltages, and the decay from peak inward current was used to calculate the time constant ($\tau_{\text{inactivation}}$) associated with channel fast inactivation. At either -15 mV or -5 mV, $\tau_{\text{inactivation}}$ in *Fhf1*^{-/-}*Fhf4*^{-/-} cells was significantly shorter than in wild-type cells (p < 0.001).

(B) Superimposed and scaled current traces from wild-type (solid line) and *Fhf1*^{-/-}*Fhf4*^{-/-} (dashed line) cells following depolarization to -5 mV illustrates the faster current decay in the mutant cell. Traces were minimally offset along x axis to visualize the similar rapid onset of sodium current.

(C–E) Recovery of sodium channels from inactivation. Superimposed current traces recorded from a wild-type neuron (C) in response to voltage commands consisting of two 10 ms depolarizations separated by variable recovery phases at -85 mV. The second peak sodium current associated with several recovery times is indicated (arrowheads). Arrow denotes resurgent sodium current accompanying repolarization. Superimposed current traces recorded from a *Fhf1*^{-/-}*Fhf4*^{-/-} neuron (D) show slower rate of recovery. (E) Percent maximal sodium channel recovery versus recovery time for wild-type (solid squares, n = 7) and *Fhf1*^{-/-}*Fhf4*^{-/-} (open squares, n = 6) cells.

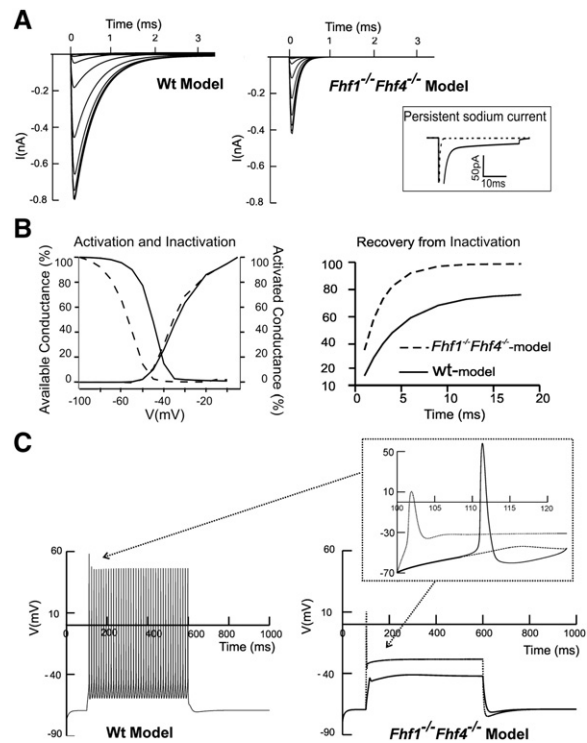


Figure 8. Computer Modeling of Intrinsic Excitability in Wild-Type and *Fhf1*^{-/-}*Fhf4*^{-/-} Granule Neurons

The kinetics of state-to-state sodium channel transitions was modeled to approximate the recorded physiological behavior of channels in wild-type and mutant neurons.

(A) Sodium currents generated in a voltage-clamp simulation from the holding potential of -80 mV to various test potentials, as indicated. Note lesser amplitude and faster inactivation kinetics in the *Fhf1*^{-/-}*Fhf4*^{-/-} mutant. The decrease of persistent sodium current in the *Fhf1*^{-/-}*Fhf4*^{-/-} mutant (dotted line) model in comparison to wild-type (solid line) model is shown in the inset.

(B) Voltage-dependent activation, inactivation, and recovery rate of sodium channels in the wild-type and *Fhf1*^{-/-}*Fhf4*^{-/-} mutant models. The voltage dependence of activation is minimally affected by mutation, while steady-state inactivation shows a 10 mV leftward shift in the *Fhf1*^{-/-}*Fhf4*^{-/-} mutant simulation. The rate of recovery from inactivation for sodium channels in the *Fhf1*^{-/-}*Fhf4*^{-/-} mutant model is slowed, analogous to channel properties in recorded cells. At 5 ms, only 50% of channels in the mutant model have recovered, while recovery is 90% in the wild-type model.

(C) Current-clamp simulation. The wild-type granule cell model shows repetitive firing upon a depolarizing current injection of 10 pA. For the *Fhf1*^{-/-}*Fhf4*^{-/-} model, sodium channel density was doubled to allow similar peak sodium conductance, as seen in some recorded neurons. Even with this compensation, firing is abolished in the mutant model at 10 pA current injection, and just a single early spike is elicited with more injected current (70 pA). $V_{\text{threshold}}$ is also higher in the *Fhf1*^{-/-}*Fhf4*^{-/-} model.

open state without modifying the voltage-dependent processes leading to channel opening, the *Fhf1*^{-/-}*Fhf4*^{-/-} model did not show appreciable shift in the voltage dependence of sodium channel activation (Figure 8B). However, since drain into the inactivated states was increased, the maximum peak conductance in the *Fhf1*^{-/-}*Fhf4*^{-/-}

model was reduced from 900 pS to 500 pS. The reduced peak sodium conductance in the mutant model is consistent with recording data from slice preparations (Table 1C), although at odds with similar peak currents recorded in physiological buffers (Table 1A) or of sodium currents recorded from cultured granule cells (Table 1B). This discrepancy leaves open the possibility that sodium channel density in mutant neurons is somewhat increased, reflecting development of compensatory mechanisms.

The model was next used to test the effects of sodium channel modification on granule cell excitability. Indeed, the changes in sodium currents were sufficient to depress spike firing in current-clamp simulations, even after normalizing the maximum sodium conductance (Figure 8C). Whereas the wild-type model fired repetitively when 10 pA current injection was simulated, the *Fhf1*^{-/-}*Fhf4*^{-/-} model cell did not fire at all. With increased injected current in the simulation, the *Fhf1*^{-/-}*Fhf4*^{-/-} model cell could generate only a first rapid-onset action potential, albeit at a higher voltage threshold (Figure 8C, inset), analogous to the excitability deficits of recorded mutant neurons.

DISCUSSION

Loss of mouse *Fhf4* function prevents prolonged repetitive firing of cerebellar granule neurons and induces ataxia, while the additional loss of *Fhf1* function exacerbates these deficits. Granule neurons relay and refine high-frequency sensory and cerebral inputs transmitted by mossy fibers and distribute this information through their parallel fibers to Purkinje cell synapses (Eccles et al., 1967). In contrast, climbing fibers in the cerebellum exert strong low-frequency inputs onto Purkinje cells. Therefore, impaired granule neuron excitability in *Fhf* mutant animals is likely to prevent high-speed information processing in the cerebellum, resulting in ataxia. Furthermore, impaired high-frequency excitation of granule cells in *Fhf* mutant animals is anticipated to interfere with plasticity of granule cell/Purkinje cell synapses, which is normally driven by burst firing of the presynaptic granule cell (Casado et al., 2002). These studies do not rule out additional requirements for FHF4s in the cerebellar circuitry mediated through potential FHF4 expression in other types of cerebellar neurons. Our findings also suggest that impaired neuronal excitability underlies a type of human spinocerebellar ataxia traced to an inherited missense mutation in the *Fhf4* gene (van Swieten et al., 2003).

The impaired excitability of *Fhf* mutant granule neurons can be explained by altered inactivation and recovery of voltage-gated sodium channels, although a role for FHF4s in the physiology of other classes of ion channels cannot be excluded. While sodium channel distribution, isotype, abundance, and voltage dependence of activation are not substantially affected by *Fhf1* and *Fhf4* mutations, sodium channels in mutant granule cells inactivate at more negative membrane potential, inactivate faster at any specific membrane potential, and are slower to recover from fast inactivation than are channels in wild-

type cells. Consistent with these findings, ectopic expression of FHF4a or FHF4b proteins in immortalized Neuro2A cultured cells or in primary hippocampal neurons induces depolarizing shifts in the voltage dependence of sodium channel inactivation (Lou et al., 2005), and transfection of FHF2 proteins into an immortalized cell line derived from sensory neurons also induces depolarizing shifts in sodium channel inactivation (Rush et al., 2006; Wittmack et al., 2004). Since FHF4s bind to sodium channel α subunits, the above findings readily suggest that sodium channels are physiologically modified through the binding of FHF4s. However, ectopic FHF4 expression studies have failed to document the role of FHF4s in accelerating sodium channel recovery from fast inactivation (Rush et al., 2006; Wittmack et al., 2004). Therefore, FHF4 modulation of sodium channels in vivo appears to be molecularly complex and as yet not fully recapitulated in ectopic gain-of-function culture systems.

An understanding of the mechanism underlying FHF4 control of sodium channel inactivation shall require further investigation. Mathematical modeling suggests that alterations in the rate constants governing the transition from closed and open states into the inactivated states is sufficient to cause the electrophysiological changes observed in *Fhf1*^{-/-}*Fhf4*^{-/-} mice. Sodium channel inactivation is governed by interaction between an inactivation "particle" housed in the III-IV cytoplasmic loop and the inner pore of the channel (Patton et al., 1993; Vassilev et al., 1988; West et al., 1992). The channel C-terminal tail also contributes to inactivation (An et al., 1998; Glaaser et al., 2006; Mantegazza et al., 2001), potentially through contacts between the tail and the III-IV loop (Motoike et al., 2004). Since the sodium channel tail is the documented site of FHF4 binding (Liu et al., 2001, 2003; Wittmack et al., 2004), FHF4s may act through modulation of interactions among channel α subunit inactivation domains or through FHF4-mediated recruitment or displacement of other channel binding proteins. In this regard, it is intriguing that inactivation of sodium channel Na_v1.1 is modulated by β subunit interaction with the Na_v1.1 C-terminal tail (Spampanato et al., 2004).

While the *Fhf4* gene plays a greater role in granule neuron excitability than does *Fhf1*, it is not clear whether FHF4 proteins are more efficient than FHF1 as modulators of sodium channels or, alternatively, if FHF4 proteins are expressed at higher levels in these cells. The broader question is to what degree excitability of different neurons is dependent on the specific *Fhf* genes and protein isoforms expressed in these cells as opposed to the mere aggregate concentration of FHF4. Resolving the question of FHF4 protein specificity awaits development of quantitative assays for FHF4 interaction with sodium channels and, more importantly, for FHF4 modulation of channel inactivation.

The behavioral deficits in *Fhf1*^{-/-}*Fhf4*^{-/-} mice extend beyond ataxia to anomalies in neuromuscular and locomotor functions. The association of other FHF4s with sodium channels at axon initial segments and at nodes

of Ranvier, together with the widespread expression of *Fhf* genes throughout the nervous system (Smallwood et al., 1996; Hartung et al., 1997; Wang et al., 2000), suggest a broad role for the FHF family of proteins in the control of intrinsic excitability and other sodium-channel-dependent processes.

EXPERIMENTAL PROCEDURES

Mutant Mice in This Study

The mouse *Fhf1* gene was isolated on a bacterial artificial chromosome by screening a genomic library with a mouse *Fhf1* cDNA (Hartung et al., 1997) hybridization probe. The gene targeting vector consisted of a 13.1 kilobase pair (kbp) region of the *Fhf1* gene in which a central 1.0 kbp segment containing coding exon 2 was replaced with a PGKneo G418 selection cassette (see Figure 1). R1 (129/Sv, agouti/agouti) embryonic stem (ES) cell G418-resistant clones transformed with the targeting cassette were screened by Southern blot hybridization to identify clones bearing a disrupted *Fhf1* allele (targeting frequency approximately 2% of clones) (see Figure 1). *Fhf1*^{+/-} ES cells were injected into C57Bl/6 blastocysts, which were reimplanted into foster mother hosts. Male chimeras were bred with C57Bl/6 females, and agouti progeny were screened by Southern blotting to identify *Fhf1*^{+/-} mice (see Figure 1). Since exon 2 is common to the two splice isoforms of *Fhf1* mRNA (Hartung et al., 1997; Schoorlemmer and Goldfarb, 2001) and encodes part of the β -trefoil fold required for FHF binding to target proteins (Liu et al., 2001, 2003; Olsen et al., 2003), the disrupted *Fhf1* allele is presumed to be functionally null.

Fhf4^{-/-} mice (from a mixed C57Bl/6 and 129/Sv background) (Wang et al., 2002) were crossed with *Fhf1*^{+/-} animals, and mutant alleles in *Fhf1*^{+/-}*Fhf4*^{+/-} progeny were propagated through two backcross generations onto a 129/Svev background before intercrossing to yield desired genotypes for analysis, including wild-type, *Fhf1*^{-/-}, *Fhf4*^{-/-}, and *Fhf1*^{-/-}*Fhf4*^{-/-}. Thereafter, wild-type and *Fhf1*^{-/-} mice were maintained as fertile colonies. For *Fhf4*^{-/-} mice, which bred poorly, and *Fhf1*^{-/-}*Fhf4*^{-/-}, which could not breed at all, desired animals were continually generated through heterozygote mating. Genotyping was performed by Southern blotting or PCR (Figure 1) (Wang et al., 2002).

Behavioral Assays

The ledge test monitored the length of time (up to a maximum of 1 min) an animal could maintain its balance on a high (35 cm), narrow (8 mm) rubber ledge, as described elsewhere (Schaefer et al., 2000).

The footprint assay was performed as described previously (Wang et al., 2002), except that hindpaws and forepaws were painted different colors to allow measurement of the polarity of paw placement disparities. For each animal, the paw placement disparity in the forward direction was measured and averaged for six consecutive steps.

The grid grip test visually monitored the ability of a mouse to maintain itself on a wire bar cage lid held to 45°, perpendicular, or inverted positions. The behaviors for each genotype tested are illustrated in the videos in Figure S1; all mice within each genotype group ($n \geq 3$) performed indistinguishably.

For the activity test, each mouse was placed in a clean 1 l glass beaker and monitored during a 1 min period for how many 360° turns it executed. After a trial acclimation day, the results from the second day were recorded. This assay was routinely performed in favor of the standard open field laser beam-monitored activity assay, since, in the latter, *Fhf1*^{-/-}*Fhf4*^{-/-} mice were hyperactive for short periods of time followed by prolonged immobility, perhaps reflecting fatigue accompanying weakness in this genotype.

Mouse Cerebellar Granule Neuron Cell Culture and Transfection

Individual mouse cerebella (postnatal day 10) were separately teased free from surrounding meninges, treated with trypsin and DNaseI, triturated, and each cell preparation plated in Dulbecco's modified

Eagle's (DME) medium + horse (5%) and fetal calf (5%) sera onto four 12 mm diameter poly-D-lysine-coated glass coverslips. The medium was changed to serum-free after 48 hr, and cells were maintained for 18 days prior to DNA transfection and for between 16–30 days prior to electrophysiological recording. Granule neurons were identified by their round, small-diameter soma and their small membrane capacitance measured in whole-cell patch-clamp (see below). Granule neurons were transfected with pEGFP-N1 vectors (Clontech) directing expression of mouse FHF1a or human FHF1b (Lou et al., 2005; Schoorlemmer and Goldfarb, 2001) fused to GFP using Lipofectamine 2000 (Invitrogen) and processed for immunofluorescence 24 hr later.

Rat Hippocampal Neuron Cell Culture

Hippocampi dissected from embryonic day 18 rats were digested with 7 Units/ml papain (Sigma Chemical) + 0.17 mg/ml L-cysteine in Hank's balanced salt solution (HBSS), then incubated with HBSS + 1 mg/ml bovine serum albumin + 1 mg/ml trypsin inhibitor followed by trituration and plating onto poly-D-lysine-coated glass coverslips (12 mm diameter) at a density of four coverslips per hippocampus in DME medium containing 5% fetal calf serum. Cells were switched to serum-free DME medium after 24 hr. Neurons were processed for immunofluorescence after 12 days in culture.

Histology and Immunofluorescence

Sagittal vibratome sections (0.25 mm thickness) of adult mouse cerebellar vermis were fixed in phosphate-buffered saline + 4% paraformaldehyde on ice for 1 hr, then cryosectioned at 15 micron thickness and stained with a combination of cresyl violet, eosin Y, and Luxol Fast blue. Sections were otherwise analyzed by immunofluorescence and confocal microscopy. Rat hippocampal neurons (12 days in vitro) and mouse transfected (20 days in vitro) and untransfected (30 days in vitro) cerebellar neurons were fixed as above and analyzed by immunofluorescence. Primary antibodies utilized were mouse monoclonal anti-pan-sodium channel α subunit (Sigma Chemical), rabbit anti-Nav1.6 (Boiko et al., 2001), rabbit anti-glutamate transporter EAAC1 (Alpha Diagnostics), rabbit anti-FHF2 (Schoorlemmer and Goldfarb, 2001), mouse monoclonal anti-ankyrin G (Santa Cruz Biotechnology), rabbit anti-microtubule associated protein-2 (MAP2, Chemicon), and mouse monoclonal anti-green fluorescent protein (Chemicon). Secondary reagents were biotinylated anti-rabbit IgG, anti-mouse IgG, and anti-mouse IgG2a (Jackson ImmunoResearch), and fluorescent reagents (Molecular Probes): anti-rabbit IgG-Alexa 488, anti-mouse IgG1-Alexa 594, streptavidin-Alexa 488, and streptavidin-Alexa 594. Cell nuclei were visualized with DAPI. Digital images were taken on a Nikon Axiophot microscope or on a Leica confocal microscope. Consecutive z axis images were stacked to allow visualization of axons running oblique to the imaging plane.

Electrophysiology

Preparation of Brain Slices and Cultured Neurons for Recordings

Adult mice (3- to 12-month-old) were anesthetized by halothane inhalation, decapitated, and their cerebellar vermis chilled with ice-cold modified Krebs's solution: 120 mM NaCl, 3 mM KCl, 1.2 mM KH₂PO₄, 26 mM NaHCO₃, 3 mM glucose, 2 mM Na pyruvate, 3 mM myo-inositol, 1.2 mM MgSO₄, 2 mM CaCl₂, 0.4 mM Na ascorbate, 0.5 mM kynurenic acid (pH 7.2). Vibratome sagittal sections (200–250 μ m thickness) were allowed to recover for at least 30 min in the same solution at room temperature continually bubbled with oxygen/carbon dioxide (95%/5%) and were then placed in the unheated recording chamber on the stage of a Nikon EF600 microscope and continuously perfused with oxygenated solutions during recordings. Alternatively, coverslips containing cerebellar granule neurons cultured for 16–30 days in vitro (see above) were directly transferred into the recording chamber.

Whole-Cell Patch-Clamp Methodology

Recordings were conducted using Axopatch 200A or 200B amplifiers interfaced to pCLAMP command/record software through a Digidata

1322 analog/digital converter (Axon Instruments/Molecular Devices). Patch pipettes were pulled to 1.0–1.5 μm tip diameter using borosilicate glass tubing (1.5 mm O.D./0.97 mm I.D.) in P-87 or P-97 pipette pullers (Sutter Instruments). For all current injection experiments and for examination of all currents in voltage clamp, pipettes were filled with 126 mM K gluconate, 4 mM NaCl, 5 mM KOH-buffered HEPES, 15 mM glucose, 1 mM MgSO₄, 0.15 mM BAPTA, 0.05 mM CaCl₂, 3 mM Mg ATP, 0.1 mM Na GTP (pH 7.2), and the tissue slice was perfused with modified Krebs's solution. For measurement of sodium currents, the pipette solution consisted of 104 mM CsF, 50 mM tetraethylammonium (TEA) Cl, 10 mM CsOH-buffered HEPES, 5 mM glucose, 2 mM MgCl₂, 10 mM EGTA, 2 mM Na ATP, 0.2 mM Na GTP (pH 7.2), and the tissues or cultured cells were perfused with 74 mM NaCl, 3 mM KCl, 26 mM NaHCO₃, 3 mM CsCl, 5 mM glucose, 25 mM TEA-Cl, 2 mM MgCl₂, 10 mM NaOH-buffered HEPES, 5 mM 4-amino-pyridine, 4 mM BaCl₂, 0.2 mM CdCl₂ (pH 7.2), as previously described (Magistretti et al., 2006), except that the perfusion solution was supplemented with 0.5 mM kynurenic acid, 2 mM Na pyruvate, 3 mM myo-inositol, and 0.4 mM Na ascorbate to limit neuronal death. Pipette resistances were 8–12 MΩ when using pipette and bath solutions for all currents or were 4–8 MΩ when using sodium-only solutions. Junctional potentials were manually offset before patching. Sealing onto granule neurons in the granule layer of slices was achieved without visual aid, while sealing onto cultured neurons was achieved while viewing cells at 400× magnification. Whole-cell access was initiated after seal resistance exceeded 8 GΩ. Recordings were filtered at 5 kHz and digitally sampled at 10 or 20 kHz. Membrane capacitance (C_m) was calculated from measurement of the area under current transients induced by 10 mV voltage-clamp steps (–85 to –75 mV or –70 to –80 mV). Series resistance was calculated based upon the measured time constant for fast decay of the capacitative current transient using the formula R_{series} = τ_{fast}/C_m, and the frequency of voltage clamp was calculated using the formula f_{VC} = 1/(6.28 × τ_{fast}). Input resistance was calculated from change in leak current using formula R_{in} = ΔV_m/ΔI_{leak}. Measured membrane voltages from current-clamp recordings were corrected by –10 mV to offset the liquid junction potential (LJP) (V_m = V_{record} + LJP), which was measured empirically as –10.1 ± 0.3 mV using the agar-bridge reference electrode method (Neher, 1992). For recordings in sodium current-only solutions, a –5 mV offset was applied to convert V_{command} to V_{membrane} (V_m = V_c + LJP), reflecting an empirically measured LJP of –5.2 ± 0.4 mV.

Induction of Action Potentials by Current Injection

A patched cell was first subjected to a multisweep voltage-clamp protocol in which membrane voltage (V_m) was stepped from –80 mV to test voltages (–70 + 10N mV, N = 1–8) for 30 ms and current was recorded. Passive current transients and leak currents were subtracted during data acquisition using a hyperpolarizing prepulse protocol (P/6). The cell was then placed under current-clamp control, V_m was adjusted to –80 mV through manual current injection, and the cell was subjected to 800 ms intervals of inward current injection of different amplitudes while recording V_m. The amplitude of current injection was increased until action potential frequency plateaued or diminished. The cell was again analyzed by voltage clamp to confirm that active currents had not substantially degraded; current injection data from a cell was only included in analyses if voltage-activated currents had diminished less than 20% from values preceding current clamp. Threshold voltage for spike generation (V_{threshold}) was determined from recorded voltage traces as the inflection point of accelerating spike

upstroke. Threshold current for spike generation (I_{threshold}) was the minimum depolarizing current needed to elicit at least one action potential. In all genotypes, V_{threshold} reflected the amount of passive depolarization generated by I_{threshold}, i.e., V_{rest} – V_{threshold} = I_{threshold} × R_{in}. Current injection excitability data are only reported for neurons in brain slice preparations; wild-type cultured granule neurons showed a deficiency in A-type potassium current resulting in reduction of spike afterhyperpolarizations and inconsistent repetitive firing.

Sodium Channel Activation

To analyze voltage dependence of sodium channel activation, cells were subjected to an 18-sweep protocol in which V_m was stepped from –85 mV to test voltages (–85 + 5N mV, N = 1–18) for 30 ms. Peak sodium current was plotted against V_m, and maximum sodium conductance computed from the linear portion of the plot (–10 to +5 mV range), enabling a plot of percentage open channels versus V_m. The data were directly fit to a Boltzmann equation with the formula

$$f(V_m) = 1 / (1 + e^{(V_{1/2(act)} - V_m)/k}),$$

where f(V_m) is the fraction of open channels, V_{1/2(act)} is the voltage of half-maximal activation, and k is the slope factor. For recordings of neurons in adult brain slices, the plot of peak conductance versus V_m showed a two-phase transition (e.g., Figures S5A and S5B) indicative of clamp escape and precluding analysis of voltage-dependent activation.

Sodium Channel Inactivation Rate

The rate constant τ_{fast} for fast inactivation of sodium channels in cultured neurons was calculated by fitting the decay from 90% to 10% peak sodium conductance to a two-component exponential decay using the formula

$$I(t) = I_{fast}(e^{-t/\tau_{fast}}) + I_2(e^{-t/\tau_2}) + C$$

τ_{fast} was only accepted for cells in which I_{fast} > 0.75 I_{total}.

Persistent Sodium Current

Following depolarization from –85 mV to –35 mV, average residual sodium current measured 25–30 ms after onset of depolarization was taken as the persistent current.

Voltage Dependence of Sodium Channel Inactivation

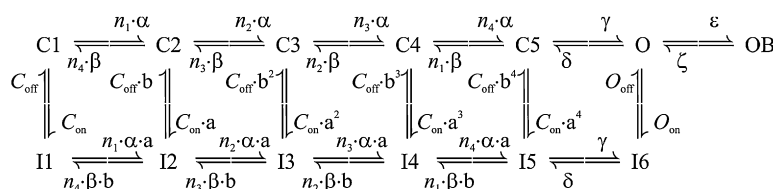
To analyze voltage dependence of sodium channel inactivation, cells were subjected to an 18-sweep protocol in which V_m was stepped from –95 mV to preconditioning test voltages (–95 + 5N mV, N = 0–17) for 125 ms followed by further depolarization to –15 mV. The peak sodium current at –15 mV measures the fraction of channels still available. The plot of percentage channels available versus V_m was fit to the Boltzmann equation with the formula

$$f(V_m) = 1 / (1 + e^{(V_{1/2(inact)} - V_m)/k}),$$

where V_{1/2(inact)} is the voltage of half-inactivation, and k is the slope factor.

Sodium Channel Recovery from Inactivation

To analyze the recovery rate of sodium channels from inactivation, cells were subjected to a 16-sweep protocol in which V_m for each sweep was stepped from –85 to –15 mV for 10 ms, returned to –85 mV for 1.5N ms (N = 1–16), then depolarized again to –15 mV. The second peak sodium current for each sweep was expressed as a percentage of maximal channel recovery and plotted versus recovery time (t). For each cell, τ_{recovery} was measured by fitting data to the formula: gNa_(available)/gNa_(maximal) = 1 – e^{–t/τ}.



Scheme 1. Kinetic Scheme of the Sodium Channel Used in the Present Simulations

The effect of this scheme on granule cell sodium currents and excitability are shown in Figure 8.

Computer Modeling

Computer simulations of granule cell electrical activity were performed in the NEURON environment (Hines and Carnevale, 1997) by employing a granule cell single-compartment model described in detail elsewhere (D'Angelo et al., 2001). The sodium current was based on the 13 state, allosteric sodium channel model of Raman and Bean (2001) in the modified form described by Khaliq et al. (2003) (Scheme 1) and subsequently implemented in granule cells by Magistretti et al. (2006): the values of the kinetic parameters in Scheme 1 were $\alpha = 353.9 \cdot \exp(V/k_{\alpha}) \text{ ms}^{-1}$, $\beta = 1.272 \cdot \exp(-V/k_{\beta}) \text{ ms}^{-1}$, $k_{\alpha} = k_{\beta} = 13.9 \text{ mV}$, $n_1 = 5.42$, $n_2 = 3.28$, $n_3 = 1.83$, $n_4 = 0.74$; $\gamma = 150 \text{ ms}^{-1}$, $\delta = 40 \text{ ms}^{-1}$, $\epsilon = 1.75 \text{ ms}^{-1}$, $\zeta = 0.0201 \cdot \exp(-V/k_{\zeta}) \text{ ms}^{-1}$, $k_{\zeta} = 25.0 \text{ mV}$; $C_{\text{on}} = 0.005 \text{ ms}^{-1}$, $C_{\text{off}} = 0.5 \text{ ms}^{-1}$, $O_{\text{on}} = 0.75 \text{ ms}^{-1}$, $O_{\text{off}} = 0.005 \text{ ms}^{-1}$, $a = (O_{\text{on}}/C_{\text{on}})^{1/4}$, $b = (O_{\text{off}}/C_{\text{off}})^{1/4}$. Sodium current was calculated as $I_{\text{Na}} = f \cdot \bar{G}_{\text{Na}} \cdot (V - V_{\text{Na}})$, where f is the fraction of channels in the open (O) state as returned by numerical resolution of Scheme 1 for time and voltage; V_{Na} , the Na^+ equilibrium potential, was +87.4 mV; and \bar{G}_{Na} , the maximal Na^+ conductance, was $13.0 \text{ mS} \cdot \text{cm}^{-2}$. To reproduce results obtained in *Fhf1*^{-/-}*Fhf4*^{-/-} mice, C_{on} and O_{on} were increased by ten times, while C_{off} was decreased to 40% of its original value. In particular, changing C_{on} and O_{on} shifted steady-state inactivation, while changing C_{off} caused the shift in recovery from inactivation. For current-clamp simulations, the density of sodium channels in the mutant model was doubled, bringing peak sodium conductance up to the level achieved in the wild-type model (as seen in actual recorded cells). In the models, temperature was set at 20°C.

Supplemental Data

The Supplemental Data for this article can be found online at <http://www.neuron.org/cgi/content/full/55/3/449/DC1>.

ACKNOWLEDGMENTS

We thank Dr. Jacopo Magistretti for invaluable discussion and for sharing research data prior to publication. We further thank Christy Pardee, Stacey Rubin, and Pasqualina Farisello for their technical assistance. This research was funded by PHS grant R01-NS39906 (M.G.), CUNY equipment grant (M.G.), and EU-SENSOPAC and CARIPLO grants (E.D.'A.).

Received: June 30, 2006

Revised: November 21, 2006

Accepted: July 3, 2007

Published: August 1, 2007

REFERENCES

- Ahern, C.A., Zhang, J.F., Wookalis, M.J., and Horn, R. (2005). Modulation of the cardiac sodium channel Nav1.5 by Fyn, a Src family tyrosine kinase. *Circ. Res.* 96, 991–998.
- An, R.H., Wang, X.L., Kerem, B., Benhorin, J., Medina, A., Goldmit, M., and Kass, R.S. (1998). Novel LQT-3 mutation affects Na^+ channel activity through interactions between alpha- and beta1-subunits. *Circ. Res.* 83, 141–146.
- Boiko, T., Rasband, M.N., Levinson, S.R., Caldwell, J.H., Mandel, G., Trimmer, J.S., and Matthews, G. (2001). Compact myelin dictates the differential targeting of two sodium channel isoforms in the same axon. *Neuron* 30, 91–104.
- Cantrell, A.R., and Catterall, W.A. (2001). Neuromodulation of Na^+ channels: an unexpected form of cellular plasticity. *Nat. Rev. Neurosci.* 2, 397–407.
- Casado, M., Isope, P., and Ascher, P. (2002). Involvement of presynaptic N-methyl-D-aspartate receptors in cerebellar long-term depression. *Neuron* 33, 123–130.
- Catterall, W.A. (2000). From ionic currents to molecular mechanisms: the structure and function of voltage-gated sodium channels. *Neuron* 26, 13–25.
- Chadderton, P., Margrie, T.W., and Hausser, M. (2004). Integration of quanta in cerebellar granule cells during sensory processing. *Nature* 428, 856–860.
- Chen, C., Bharucha, V., Chen, Y., Westenbroek, R.E., Brown, A., Malhotra, J.D., Jones, D., Avery, C., Gillespie, P.J., 3rd, Kazen-Gillespie, K.A., et al. (2002). Reduced sodium channel density, altered voltage dependence of inactivation, and increased susceptibility to seizures in mice lacking sodium channel beta 2-subunits. *Proc. Natl. Acad. Sci. USA* 99, 17072–17077.
- D'Angelo, E., De Filippi, G., Rossi, P., and Taglietti, V. (1998). Ionic mechanism of electroresponsiveness in cerebellar granule cells implicates the action of a persistent sodium current. *J. Neurophysiol.* 80, 493–503.
- D'Angelo, E., Nieuw, T., Maffei, A., Armano, S., Rossi, P., Taglietti, V., Fontana, A., and Naldi, G. (2001). Theta-frequency bursting and resonance in cerebellar granule cells: experimental evidence and modeling of a slow K^+ -dependent mechanism. *J. Neurosci.* 21, 759–770.
- Eccles, J.C., Sasaki, K., and Strata, P. (1967). Interpretation of the potential fields generated in the cerebellar cortex by a mossy fibre volley. *Exp. Brain Res.* 3, 58–80.
- Gall, D., Roussel, C., Susa, I., D'Angelo, E., Rossi, P., Bearzatto, B., Galas, M.C., Blum, D., Schurmans, S., and Schiffmann, S.N. (2003). Altered neuronal excitability in cerebellar granule cells of mice lacking calcitriol. *J. Neurosci.* 23, 9320–9327.
- Glaaser, I.W., Bankston, J.R., Liu, H., Tateyama, M., and Kass, R.S. (2006). A carboxyl-terminal hydrophobic interface is critical to sodium channel function. Relevance to inherited disorders. *J. Biol. Chem.* 281, 24015–24023.
- Goldfarb, M. (2005). Fibroblast growth factor homologous factors: evolution, structure, and function. *Cytokine Growth Factor Rev.* 16, 215–220.
- Grieco, T.M., Malhotra, J.D., Chen, C., Isom, L.L., and Raman, I.M. (2005). Open-channel block by the cytoplasmic tail of sodium channel beta4 as a mechanism for resurgent sodium current. *Neuron* 45, 233–244.
- Hartung, H., Feldman, B., Lovic, H., Coulier, F., Birnbaum, D., and Goldfarb, M. (1997). Murine FGF-12 and FGF-13: expression in embryonic nervous system, connective tissue and heart. *Mech. Dev.* 64, 31–39.
- Herzog, R.I., Cummins, T.R., Ghassemi, F., Dib-Hajj, S.D., and Waxman, S.G. (2003). Distinct repriming and closed-state inactivation kinetics of Nav1.6 and Nav1.7 sodium channels in mouse spinal sensory neurons. *J. Physiol.* 551, 741–750.
- Hines, M.L., and Carnevale, N.T. (1997). The NEURON simulation environment. *Neural Comput.* 9, 1179–1209.
- Isom, L.L., Scheuer, T., Brownstein, A.B., Ragsdale, D.S., Murphy, B.J., and Catterall, W.A. (1995). Functional co-expression of the beta 1 and type IIA alpha subunits of sodium channels in a mammalian cell line. *J. Biol. Chem.* 270, 3306–3312.
- Khaliq, Z.M., Gouwens, N.W., and Raman, I.M. (2003). The contribution of resurgent sodium current to high-frequency firing in Purkinje neurons: an experimental and modeling study. *J. Neurosci.* 23, 4899–4912.
- Kordeli, E., Lambert, S., and Bennett, V. (1995). AnkyrinG. A new ankyrin gene with neural-specific isoforms localized at the axonal initial segment and node of Ranvier. *J. Biol. Chem.* 270, 2352–2359.
- Liu, C., Dib-Hajj, S.D., and Waxman, S.G. (2001). Fibroblast growth factor homologous factor 1B binds to the C terminus of the tetrodotoxin-resistant sodium channel rNav1.9a (NaN). *J. Biol. Chem.* 276, 18925–18933.

- Liu, C.J., Dib-Hajj, S.D., Renganathan, M., Cummins, T.R., and Waxman, S.G. (2003). Modulation of the cardiac sodium channel Nav1.5 by fibroblast growth factor homologous factor 1B. *J. Biol. Chem.* 278, 1029–1036.
- Lou, J.Y., Laezza, F., Gerber, B.R., Xiao, M., Yamada, K.A., Hartmann, H., Craig, A.M., Nerbonne, J.M., and Ornitz, D.M. (2005). Fibroblast growth factor 14 is an intracellular modulator of voltage-gated sodium channels. *J. Physiol.* 569, 179–193.
- Magistretti, J., Castelli, L., Forti, L., and D'Angelo, E. (2006). Kinetic and functional analysis of transient, persistent and resurgent sodium currents in rat cerebellar granule cells in situ: an electrophysiological and modelling study. *J. Physiol.* 573, 83–106.
- Mantegazza, M., Yu, F.H., Catterall, W.A., and Scheuer, T. (2001). Role of the C-terminal domain in inactivation of brain and cardiac sodium channels. *Proc. Natl. Acad. Sci. USA* 98, 15348–15353.
- Motoike, H.K., Liu, H., Glaaser, I.W., Yang, A.S., Tateyama, M., and Kass, R.S. (2004). The Na⁺ channel inactivation gate is a molecular complex: a novel role of the COOH-terminal domain. *J. Gen. Physiol.* 123, 155–165.
- Neher, E. (1992). Correction for liquid junction potentials in patch clamp experiments. In *Methods in Enzymol.*, B. Rudy and L. Iverson, eds. (San Diego: Academic Press), pp. 123–131.
- Olsen, S.K., Garbi, M., Zampieri, N., Eliseenkova, A.V., Ornitz, D.M., Goldfarb, M., and Mohammadi, M. (2003). Fibroblast growth factor (FGF) homologous factors share structural but not functional homology to FGFs. *J. Biol. Chem.* 278, 34226–34236.
- Ornitz, D.M., and Itoh, N. (2001). Fibroblast growth factors. *Genome Biol.* 2, reviews3005.1–reviews3005.12.
- Osorio, N., Alcaraz, G., Padilla, F., Couraud, F., Delmas, P., and Crest, M. (2005). Differential targeting and functional specialization of sodium channels in cultured cerebellar granule cells. *J. Physiol.* 569, 801–816.
- Patton, D.E., West, J.W., Catterall, W.A., and Goldin, A.L. (1993). A peptide segment critical for sodium channel inactivation functions as an inactivation gate in a potassium channel. *Neuron* 11, 967–974.
- Patton, D.E., Isom, L.L., Catterall, W.A., and Goldin, A.L. (1994). The adult rat brain beta 1 subunit modifies activation and inactivation gating of multiple sodium channel alpha subunits. *J. Biol. Chem.* 269, 17649–17655.
- Raman, I.M., and Bean, B.P. (2001). Inactivation and recovery of sodium currents in cerebellar Purkinje neurons: evidence for two mechanisms. *Biophys. J.* 80, 729–737.
- Rush, A.M., Wittmack, E.K., Tyrrell, L., Black, J.A., Dib-Hajj, S.D., and Waxman, S.G. (2006). Differential modulation of sodium channel Na(v)1.6 by two members of the fibroblast growth factor homologous factor 2 subfamily. *Eur. J. Neurosci.* 23, 2551–2562.
- Schaefer, M.L., Wong, S.T., Wozniak, D.F., Muglia, L.M., Liauw, J.A., Zhuo, M., Nardi, A., Hartman, R.E., Vogt, S.K., Luedke, C.E., et al. (2000). Altered stress-induced anxiety in adenylyl cyclase type VIII-deficient mice. *J. Neurosci.* 20, 4809–4820.
- Schoorlemmer, J., and Goldfarb, M. (2001). Fibroblast growth factor homologous factors are intracellular signaling proteins. *Curr. Biol.* 11, 793–797.
- Smallwood, P.M., Munoz-Sanjuan, I., Tong, P., Macke, J.P., Hendry, S.H., Gilbert, D.J., Copeland, N.G., Jenkins, N.A., and Nathans, J. (1996). Fibroblast growth factor (FGF) homologous factors: new members of the FGF family implicated in nervous system development. *Proc. Natl. Acad. Sci. USA* 93, 9850–9857.
- Spampanato, J., Kearney, J.A., de Haan, G., McEwen, D.P., Escayg, A., Aradi, I., MacDonald, B.T., Levin, S.I., Soltesz, I., Benna, P., et al. (2004). A novel epilepsy mutation in the sodium channel SCN1A identifies a cytoplasmic domain for beta subunit interaction. *J. Neurosci.* 24, 10022–10034.
- van Swieten, J.C., Brusse, E., de Graaf, B.M., Krieger, E., van de Graaf, R., de Koning, I., Maat-Kievit, A., Leegwater, P., Dooijes, D., Oostra, B.A., and Heutink, P. (2003). A mutation in the fibroblast growth factor 14 gene is associated with autosomal dominant cerebral ataxia. *Am. J. Hum. Genet.* 72, 191–199.
- Vassilev, P., Scheuer, T., and Catterall, W.A. (1988). Identification of an intercellular peptide segment involved in sodium channel inactivation. *Science* 241, 1658–1661.
- Wang, Q., McEwen, D.G., and Ornitz, D.M. (2000). Subcellular and developmental expression of alternatively spliced forms of fibroblast growth factor 14. *Mech. Dev.* 90, 283–287.
- Wang, Q., Bardgett, M.E., Wong, M., Wozniak, D.F., Lou, J., McNeil, B.D., Chen, C., Nardi, A., Reid, D.C., Yamada, K., and Ornitz, D.M. (2002). Ataxia and paroxysmal dyskinesia in mice lacking axonally transported FGF14. *Neuron* 35, 25–38.
- West, J.W., Patton, D.E., Scheuer, T., Wang, Y., Goldin, A.L., and Catterall, W.A. (1992). A cluster of hydrophobic amino acid residues required for fast Na⁺ channel inactivation. *Proc. Natl. Acad. Sci. USA* 89, 10905–10909.
- Wittmack, E., Rush, A.M., Craner, M.J., Goldfarb, M., Waxman, S.G., and Dib-Hajj, S.D. (2004). Fibroblast growth factor homologous factor 2B: Association with Nav1.6 and selective colocalization at nodes of Ranvier of dorsal root axons. *J. Neurosci.* 24, 6765–6775.
- Wittmack, E.K., Rush, A.M., Hudmon, A., Waxman, S.G., and Dib-Hajj, S.D. (2005). Voltage-gated sodium channel Nav1.6 is modulated by p38 mitogen-activated protein kinase. *J. Neurosci.* 25, 6621–6630.
- Wozniak, D.F., Xiao, M., Xu, L., Yamada, K.A., and Ornitz, D.M. (2007). Impaired spatial learning and defective theta burst induced LTP in mice lacking fibroblast growth factor 14. *Neurobiol. Dis.* 26, 14–26.